

# Cell segmentation from telecentric bright-field transmitted light microscopic images using a Residual Attention U-Net: a case study on HeLa line

Ali Ghaznavi<sup>a</sup>, Renata Rychtáriková<sup>a</sup>, Mohammadmehdi Saberioon<sup>b</sup>, Dalibor Štys<sup>a</sup>

<sup>a</sup>*Faculty of Fisheries and Protection of Waters, South Bohemian Research Center of Aquaculture and Biodiversity of Hydrocenoses, Institute of Complex Systems, University of South Bohemia in České Budějovice, Zámek 136, 373 33 Nové Hradky, Czech Republic*

<sup>b</sup>*Section 1.4 Remote Sensing and Geoinformatics, Helmholtz Centre Potsdam GFZ German Research Centre for Geosciences, Telegrafenberg, Potsdam 14473, Germany*

---

## Abstract

Living cell segmentation from bright-field light microscopic images is challenging due to the image complexity and temporal changes in the living cells. Recently developed deep learning (DL)-based methods became popular in medical and microscopic image segmentation tasks due to their success and promising outcomes. The main objective of this paper is to develop a deep learning, U-Net-based method to segment the living cells of the HeLa line in bright-field transmitted light microscopy. To find the most suitable architecture for our datasets, we have proposed a residual attention U-Net and compared it with an attention and a simple U-Net architecture.

The attention mechanism highlights the remarkable features and suppresses activations in the irrelevant image regions. The residual mechanism overcomes with vanishing gradient problem. The Mean-IoU score for our datasets reaches 0.9505, 0.9524, and 0.9530 for the simple, attention, and residual attention U-Net, respectively. We achieved the most accurate semantic segmentation results in the Mean-IoU and Dice metrics by applying the residual and attention mechanisms together. The watershed method applied to this best – Residual Attention – semantic segmentation result gave the segmentation with the specific

---

*Email address:* rrychtarikova@frov.jcu.cz (Renata Rychtáriková)

information for each cell.

*Keywords:* Deep Learning, Neural Network, Cell Detection, Microscopy Image segmentation, Tissue segmentation, Semantic Segmentation, Watershed segmentation

---

## 1. Introduction

Image object detection and segmentation can be defined as a procedure to localize a region of interest (ROI) in an image and separate an image foreground from its background using image processing and/or machine learning approaches. Cell detection and segmentation are the primary and critical steps in microscopic image analysis. These processes play an important role in estimating the number of the cells, initializing cell segmentation, tracking, and extracting features necessary for further analysis. We categorize the segmentation methods as 1) traditional, feature- and machine learning (ML)-based methods and 2) deep learning (DL)-based methods.

### 1.1. Traditional cell segmentation methods

Traditional segmentation methods have achieved impressive results in cell boundary detection and segmentation, with an efficient processing time [1, 2]. These methods include low-level pixel processing approaches. The region-based methods are more robust than the threshold-based segmentation methods [2]. However, in low-contrast images, cells placed close together or flat cell regions can be segmented as blobs. Rojas-Moraleda et al. [1] proposed a region-based method on the principles of persistent homology with an overall accuracy of 94.5%. The iterative morphological and Ultimate Erosion [3, 4] suffer from poor segment performance when facing small and low-contrast objects. Guan et al. [5] detected rough circular cell boundaries using the Hough transform and the exact cell boundaries using fuzzy curve tracing. Compared with the watershed-based method [6], this method was more robust to the noise and the uneven brightness in the cells. Winter et al. [7] combined the image Euclidean

distance transformation with the Gaussian mixture model to detect elliptical cells. This method requires solid objects for computing the distance transform. The target objects' large holes or extreme internal irregularities make the distance transform unreliable and reduce the method performance. Buggenthin et al. [8] identified nearly all cell bodies and segmented multiple cells instantly in bright-field time-lapse microscopy images by a fast, automatic method combining the Maximally Stable Extremal Regions (MSER) with the watershed method. The main challenges for this method remain the oversegmentation and poor performance for out-of-focus images.

The machine learning methods have expanded due to the microscopic images' complexity and the previous methods' low performance to detect and segment cells. The ML methods can be classified into two groups: supervised vs unsupervised. The supervised methods produce a mathematical function or model from the training data to map a new data sample [9]. Mualla et al. [10] utilized the Scale Invariant Feature Transform (SIFT) as a feature extractor and the Balanced Random Forest as a classifier to calculate the descriptive cell keypoints. The SIFT descriptors are invariant to illumination conditions, cell size, and orientation. Tikkanen et al. [11] developed a method based on the Histogram of Oriented Gradients (HOG) and the Support Vector Machine (SVM) to extract feature descriptors and classify them as a cell or a non-cell in bright-field microscopic data. The proposed method is susceptible to the number of iterations in the training process as a crucial step to eliminating false positive detections.

The unsupervised ML algorithms require no pre-assigned labels or scores for the training data [12]. The best known unsupervised methods are clustering methods. Mualla et al. [13] segmented unstained cells in bright-field micrographs using a combination of a SIFT to extract key points, a self-labelling, and two clustering methods. This method is fast and accurate but sensitive to the feature selection step to avoid overfitting.

### *1.2. Deep Learning cell segmentation methods*

In the last decade, Deep Learning has emerged as a new area of machine learning. The DL methods contain a class of ML techniques that exploit many layers of non-linear information processing for supervised or unsupervised feature extraction and transformation for pattern analysis and classification. The Deep Convolutional Networks exhibited impressive performance in many visual recognition tasks [14]. Song et al. [15] used a multiscale convolutional network (MSCN) to extract scale-invariant features and graph-partitioning method for accurate segmentation of cervical cytoplasm and nuclei. This method significantly improved the Dice metric and standard deviation compared with similar methods. Xing et al. [16] also proposed an automated nucleus segmentation method based on a deep convolutional neural network (DCNN) to generate a probability map. However, the proposed mitosis counting remains laborious and subjective to the observer.

One of the most popular models for semantic segmentation is Fully Convolutional Network (FCN) architectures. The FCN combines deep semantic information with a shallow appearance to achieve satisfactory segmentation results. The convolutional networks can take the arbitrary size of input images to train end-to-end, pixel-to-pixel, and produce an output of the corresponding size with efficient inference and learning to achieve semantic segmentation in complex images, including microscopic and medical images [17, 18]. Ronneberger et al. [19] proposed a training strategy that relies on the strong use of data augmentation by applying U-Net Neural Network, contracting the path to capture context, and expanding the path symmetrically to achieve a precise localization. This method was optimized with a low amount of training labelled samples and efficiently performed electron microscopic image segmentation.

As described above, traditional ML methods are not much efficient to segment cells in a microscopic image with a complex background, particularly bright-field microscopy tiny cells [8, 11, 13]. These methods cannot build sufficient models for big datasets. On the other hand, some Convolution Neural Networks (CNNs) require a vast number of manually labelled training datasets

and higher computational costs compared with the ML methods [17, 20].

Deep learning-based methods have delivered better outcomes in segmentation tasks than other methods. Therefore, the main objective of our research is to propose a highly accurate and reasonably computationally cost deep learning-based method to segment human HeLa cells in unique telecentric bright-field transmitted light microscopic images. We chose the U-Net since it is one of the most promising methods used in semantic segmentation [19]. To find the most suitable architecture for our datasets, we examined different U-Net architectures, such as Attention and Residual Attention U-Net.

## 2. Materials and methods

### 2.1. Cell preparation and microscope specification

Human HeLa cell line was growing to low optical density overnight at 37°C, 5% CO<sub>2</sub>, and 90% RH. The nutrient solution consisted of DMEM (87.7%) with high glucose (>1 g L<sup>-1</sup>), fetal bovine serum (10%), antibiotics and antimycotics (1%), L-glutamine (1%), and gentamicin (0.3%; all purchased from Biowest, Nuaille, France). The HeLa cells were maintained in a Petri dish with a cover glass bottom and lid at room temperature of 37°C when we were running experiments during data collection phase in different time laps experiments.

We captured time-lapse image series of living human HeLa cells using a high-resolved bright-field light microscope for observation of sub-microscopic objects and cells. This microscope was designed by the Institute of Complex System (ICS, Nové Hradý, Czech Republic) and built by Optax (Prague, Czech Republic) and ImageCode (Brloh, Czech Republic) in 2021. The microscope has a simple construction of the optical path. The light from two light-emitting diodes CL-41 (Optika Microscopes, Ponteranica, Italy) was passing through a sample to reach a telecentric measurement objective TO4.5/43.4-48-F-WN (Vision & Control GmbH, Shul, Germany) and an Arducam AR1820HS 1/2.3-inch 10-bit RGB camera with a chip of 4912×3684 pixel resolution. The images were captured as a primary (raw) signal with theoretical pixel size (size of the object

projected onto the camera pixel) of 113 nm. The software (developed by the ICS) controls to capture the primary signal with the camera exposure of 2.75 ms. All the experiments we performed in time-lapse to observe cells' behaviour over time.

## 2.2. Data acquisition

We completed different time-lapse experiments on the HeLa cells under the bright-field microscope (Sect. 2.1). The algorithm proposed in [21] was fully automated and implemented in the microscope control software to calibrate the microscope optical path and correct all image series to avoid image background inhomogeneities and noise.

After the image calibration, we converted the raw image representations to quarter-resolved 8-bit colour (rgb) mode with the usage of quadruplets of Bayer mask pixels [22]: We adopted red and blue camera filter pixels into the relevant image channel and averaged each pair of green camera filter pixels to create the green image channel. Then, we rescaled images to 8-bits after creating the image series intensity histogram and omitting unoccupied intensity levels. This bit reduction ensured the maximal information preservation and mutual comparability of the images through the time-lapse series.

The means denoising method [23] minimized the background noise in the constructed RGB images at preserving the texture details. Afterwards, we cropped the image series to the  $1024 \times 1024$  pixel size. We obtained 500 images from different time-lapse experiments by the steps described above.

The cells in the images were labelled manually by MATLAB (MathWorks Inc., Natick, Massachusetts, USA) as Ground-Truth (GT) single class masks with the dimension of  $1024 \times 1024$  (Fig. 1). We used the labelled images as training, testing, and evaluation sets for the proposed U-Net networks (with images of the size of  $512 \times 512$ ).

## 2.3. U-Net Model Architectures

The U-Net [19] is a semantic segmentation method proposed on the FCN architecture. The FCN consists of a typical encoder-decoder convolutional net-

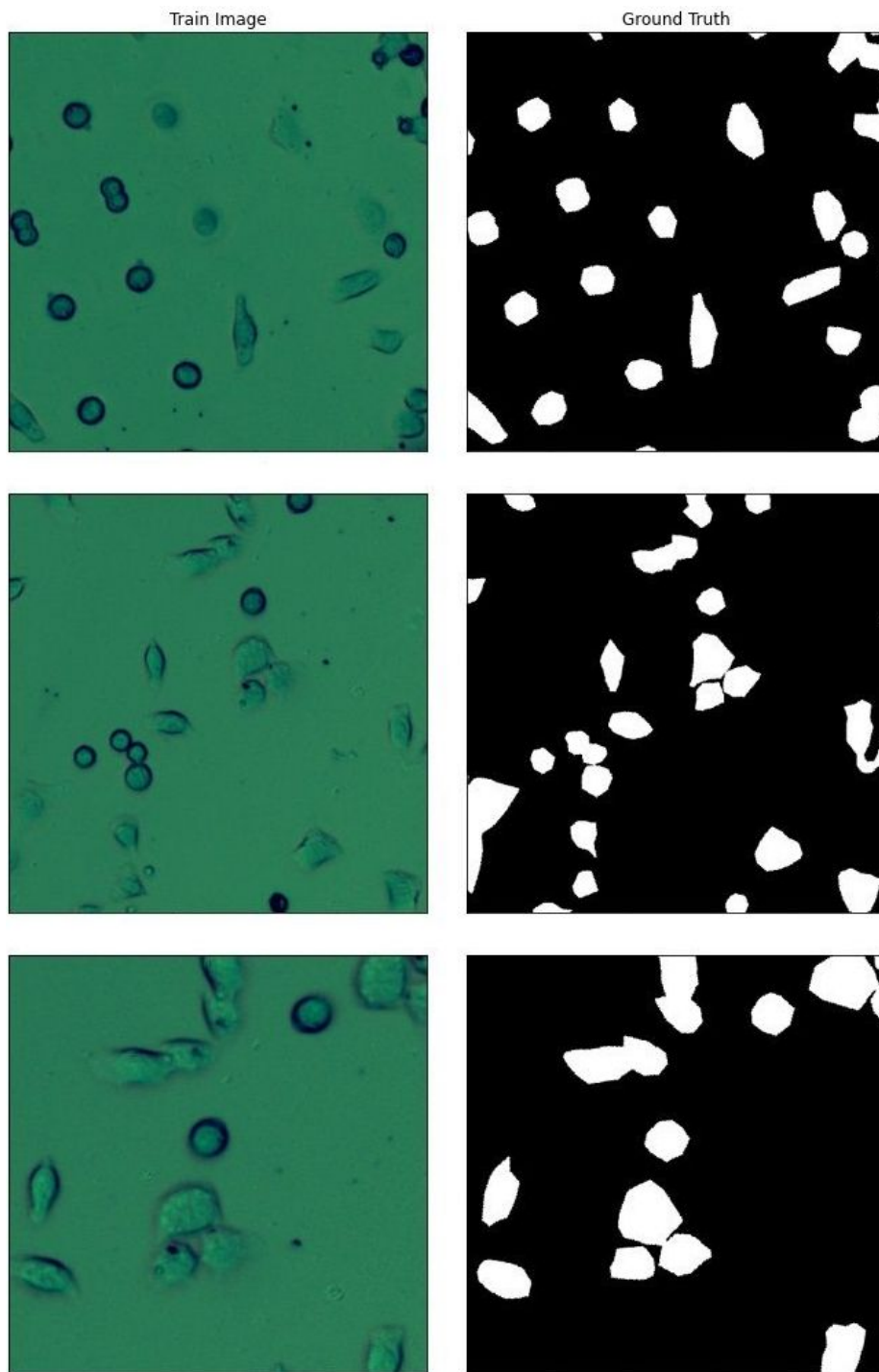


Figure 1: Examples of the train set and their ground truths. The image size is  $512 \times 512$ .

work. This architecture includes several feature channels to combine shallow and deep features. The deep features are used for positioning, whereas the shallow features are utilized for precise segmentation. We choose the architecture of simple U-Net (Fig. 2) for training the model with the specific size of input images.

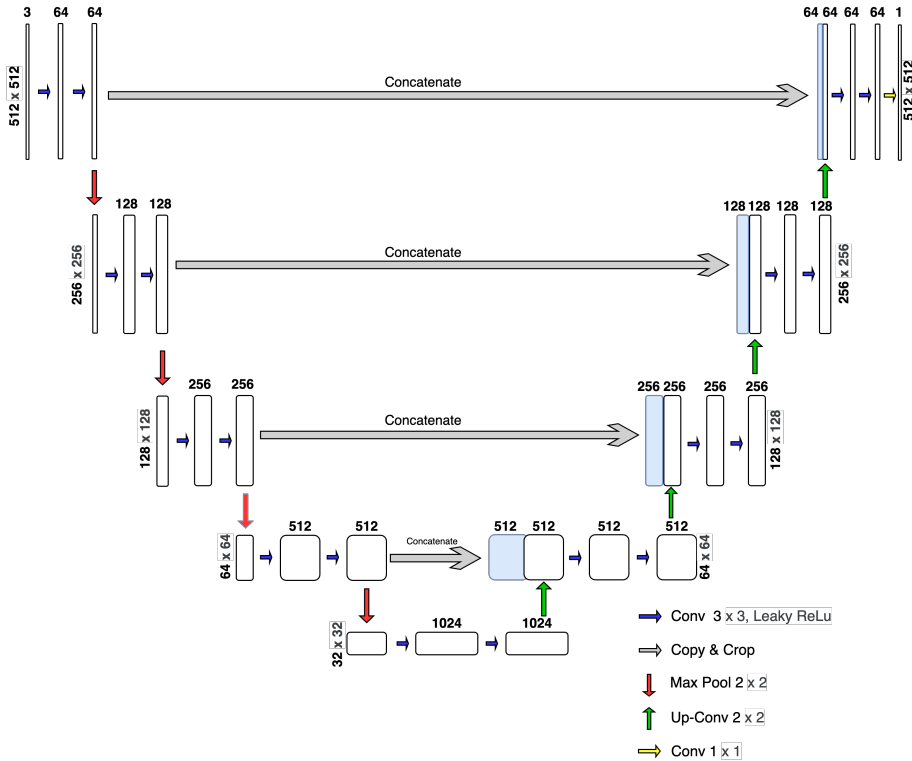


Figure 2: Architecture of the proposed simple U-Net model.

The first layer of the encoder part consists of the input layer, which accepts RGB images with the size  $512 \times 512$ . Each level in the five-”level” U-Net structure includes two  $3 \times 3$  convolutions. Batch normalization follows each convolution, and ”LeakyReLU” activation functions follow a rectified linear unit. In the down-sampling (encoder) part (Fig. 2, left part), each ”level” in the encoder consists of a  $2 \times 2$  max pooling operation with the stride of two. The max-pooling process extracts the maximal value in the  $2 \times 2$  area. By completing



down-sampling in each level of the encoder part, convolutions will double the number of feature channels.

In the up-sampling (decoder) section (Fig. 2, right part), the height and width of the exciting feature maps are doubled in each level from bottom to top. Then, the high-resolution deep semantic and shallow features were combined and concatenated with the feature maps from the encoder section. After concatenation, the output feature maps have channels twice the size of the input feature maps. The output decoder layer at the top with a  $1 \times 1$  convolution size predicts the probabilities of pixels. We consider padding in the convolution process to achieve the same input and output layers size. The computational result, combined with the Binary Focal Loss function, becomes the energy function of the U-Net.

Between each Encoder-Decoder layer in the simple U-Net (Fig. 2), there is a connection combining the down-sampling path with the up-sampling path to achieve the spatial information. Nevertheless, at the same time, this process brings also many irrelevant feature representations from the initial layers. We applied the Attention U-Net architecture (Fig. 3-A) with an impressive performance in medical imaging [24] to prevent this problem and improve semantic segmentation result achieved by standard U-Net. As an extension to the standard U-Net model architecture, the attention gate at the skip connections between encoder and decoder layers highlights the remarkable features and suppresses activations in the irrelevant regions. In this way, the attention gate improves model sensitivity and performance without requiring complicated heuristics.

The attention gate (Fig. 3-B) has two inputs  $x$  and  $g$ . Input  $x$  comes from the skip connection from the encoder layers. Since it comes from the early layers, it contains better spatial information. Input  $g$ —a gating signal—comes from the deeper network layer and contains a better feature representation. The attention part weights different parts of the images. This process will add the weights to the pixels based on their relevance in training steps. The relevant part of the image will get large weights than the less relevant parts. The

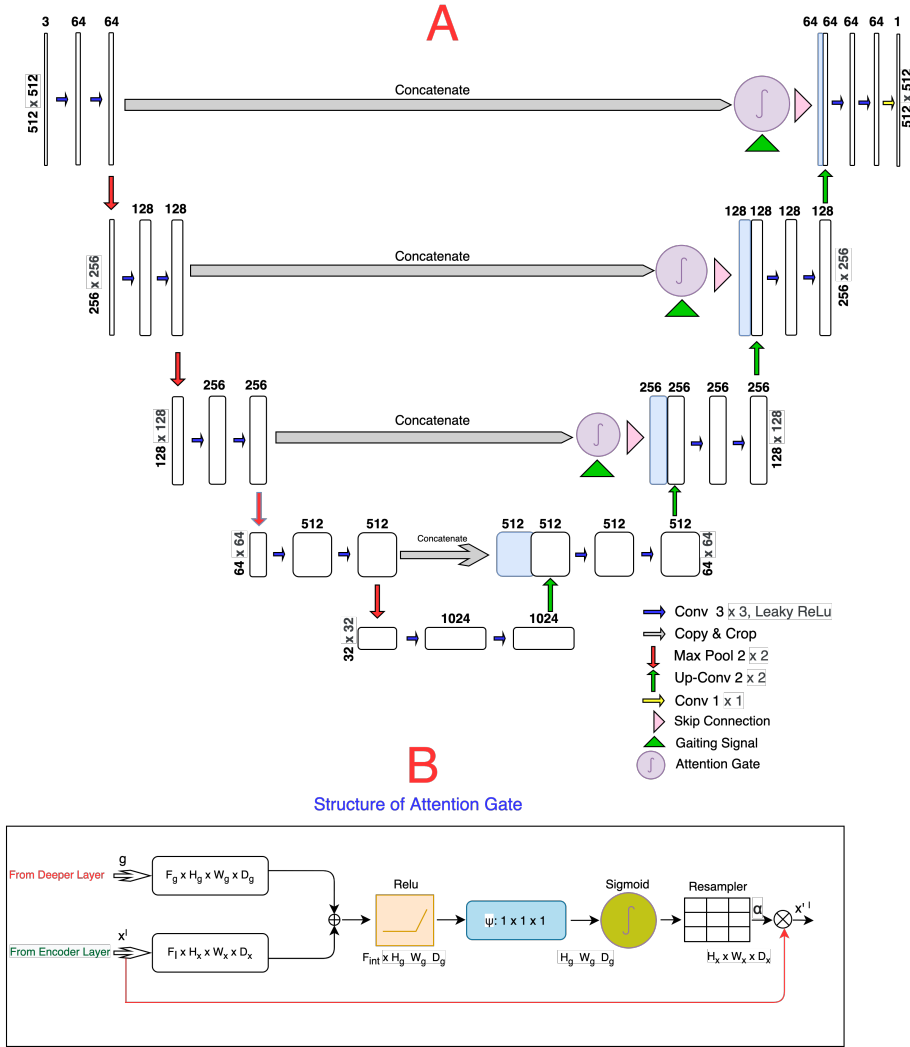


Figure 3: A) Architecture of the proposed Attention U-Net model, B) the attentive module mechanism. The size of each feature map is shown in  $H \times W \times D$ , where  $H$ ,  $W$ , and  $D$  indicate height, width, and number of channels, respectively.

achieved weights get also trained in the training process and make the trained model more attentive to the relevant regions.

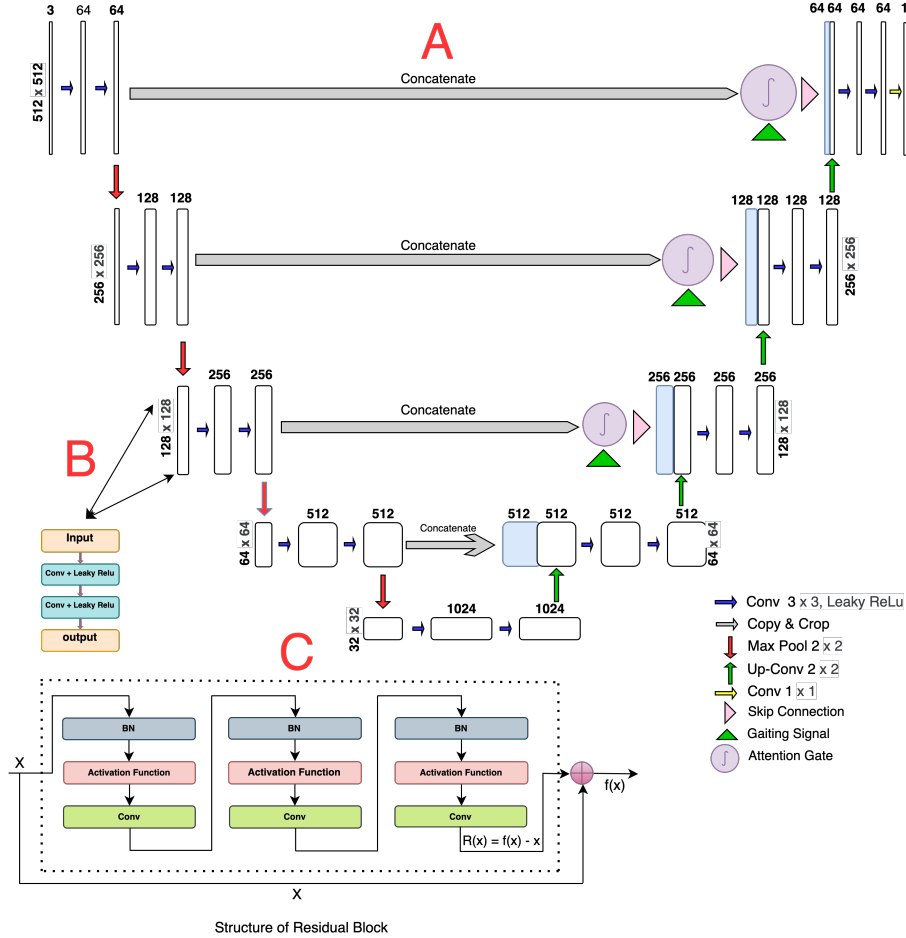


Figure 4: (A) Architecture of the Residual Attention U-Net model. (B) Each U-Net layer structure. (C) The sample of residual block progress. *BN* refers to Batch Normalization.

Another architecture used in this study and developed based on the U-Net models (originally for nuclei segmentation [25]) is the Residual U-Net. The simple U-Net architecture was built based on repetitive Convolutional blocks in each level (Fig. 4-B). Each of these Convolutional blocks consists of the input, two steps of the convolution operation followed by the activation function and the output. On the other hand, we face the vanishing gradient problem when

dealing with very deep convolutional networks. We applied the residual step to update the weights in each convolutional block incrementally and continuously (Fig. 4-C) to enhance the U-Net architecture performance by overcoming the vanishing gradient problems.

In the traditional neural networks, each convolutional blocks feed the next blocks. The other problem in a DCNN-based network, such as stacking convolutional layers, is that a deeper structure of these kind of networks will affect generalization ability. To overtake this problem, the skip connections—the residual blocks—improve the network performance, with each layer feeding the next layer and layers about two or three steps apart (Fig. 4-C). We connected the Residual and Attention U-Net architecture to build more effective and high-performance models from our datasets and improve segmentation results.

Table 1: Number of the trainable parameters and the run time for each U-Net model.

<b>Network</b>	<b>Run time</b>	<b>Training parameter</b>
<b>U-Net</b>	3:42:18"	31,402,501
<b>Attention U-Net</b>	4:04:23"	34,334,665
<b>Residual Att U-Net</b>	4:11:24"	39,090,377

After completion of the semantic segmentation by U-Net methods described above, we applied the watershed algorithm based on morphological reconstruction [26]. We first transformed the U-net semantic segmentation result into a binary image using the Otsu method [27]. After that, we determined the background regions by binary image dilation. Then, the distance transform was applied to define the foreground eroded cell regions. The unknown region was achieved by diffraction of the particular foreground region from the sure background. The watershed method applied to the unknown regions separated the cell borders. The watershed segmentation further helped us solve the over and under-segmented regions and specify each individual separated cell by, e.g., cell diameters, solidity, or mean intensity. We optimized the segmentation results by the marked images. Wrongly detected residual connections between different cell regions were cut off, which improved the method accuracy. Figure 5

presents a general diagram of the proposed U-Net based methods.

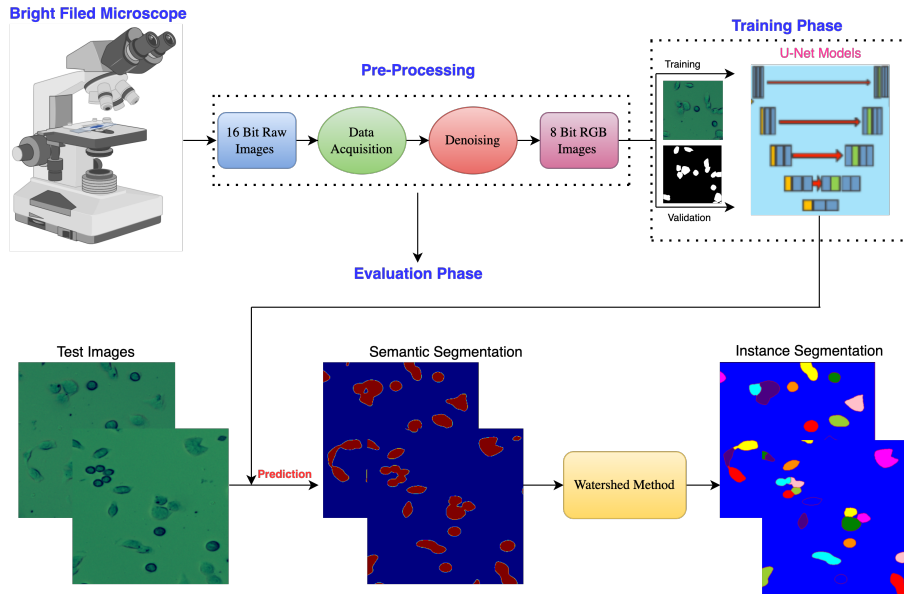


Figure 5: Flowchart of methodology applied in this study.

#### 2.4. Training Models

The computation was implemented in Python 3.7. The framework for deep learning was Keras, and the backend was Tensorflow [28]. The whole method, including the Deep Learning framework, was transferred and executed on the Google Colab Pro account with P100 and T4 GPU, 24 Gb of RAM, and 2 vCPU [29]. After data preprocessing (Sect. 2.2), we divided the primary dataset into training (80%) and test (20%). A part (20%) of the training set was used for model validation in the training process to avoid over-fitting and achieve higher performance. Among a 500-image dataset of the mixture of under-, over-, and focused images, 320 images were randomly selected to train the model, and 80 images were chosen randomly to validate the process. The rest of the 100 dataset images were considered for testing and evaluating the model after training.

Before the training, the images were normalized: the pixel values were rescaled in the range from 0 to 1. Since all designed network architectures

work with a specific input image size, all datasets were resized to  $512 \times 512$  pixel size. We also applied data augmentation parameters for training all three U-Net architectures. The optimized values of the hyperparameters used in the training process are written in Tab. 2. The "rotation range" represents an angle of the random rotation, "width shift range" represents an amplitude of the random horizontal offset, "height shift range" corresponds to an amplitude of the random vertical offset, "shear range" is a degree of the random shear transformation, "zoom range" represents a magnitude of the random scaling of the image. We applied Early Stopping hyperparameters to avoid over-fitting during the model training and the patient value was considered as 15. The activation function was set to the LeakyRelu, and the Batch size was set to 8. To optimize the network, we chose the Adam optimizer and set the learning rate to  $10^{-3}$ .

Table 2: Hyperparameters setting for all three U-Net models.

Parameter name	Value
Activation function	LeakyRelu
Learning rate	$10^{-3}$
Batch size	8
Epochs number	100
Early stop	15
Step per epoch	100
Rotation range	90
Width shift range	0.3
Height shift range	0.3
Shear range	0.5
Zoom range	0.3

We can consider semantic image segmentation as a pixel classification as either the cell or background class. The Dice loss was used to compare the segmented cell image with the GT and minimize the difference between them as much as possible in the training process. One of the famous loss functions used for semantic segmentation is the Binary Focal Loss (Eq. 1) [30]:

$$\text{Focal Loss} = -\alpha_t(1 - p_t)^\gamma \log(p_t), \quad (1)$$

where  $p_t \in [0, 1]$  is the model’s estimated probability for the GT class with label  $y = 1$ ; a weighting factor  $\alpha_t \in [0, 1]$  for class 1 and  $1 - \alpha_t$  for class  $-1$ ;  $\gamma \geq 0$  is a tunable focusing parameter. The focal loss can be enhanced by the contribution of hardly segmented regions (e.g., cells with vanish borders) and distinguish parts between the background and the cells with unclear borders. The second benefit of the focal loss is that it controls and limits the contribution of the easily segmented pixel regions (e.g., sharp and apparent cells) in the image at the loss of the model. In the final step, updating the gradient direction is under the control of the model algorithm, dependent on the loss of the model.

### 2.5. Evaluation metrics

We used different metrics (Eqs. 2–6, where TP, FP, FN and TN are true positive, false positive, false negative, and true negative metrics, respectively), to evaluate our proposed semantic segmentation based models [31]. The metrics were computed for all test sets and explained as mean values (Tab. 3).

Overall pixel accuracy (Acc) represents a per cent of image pixels belonging to the correctly segmented cells. Precision (Pre) is a proportion of the cell pixels in the segmentation results that match the GT. The Pre, known as a positive predictive value, is a valuable metric for the segmentation performance because it is sensitive to over-segmentation. Recall (Recl) represents the proportion of cell pixels in the GT correctly identified through the segmentation process. This metric says what proportion of the objects annotated in the GT was captured as a positive prediction. The Pre and Recl together give an important metric—F1 score—to evaluate the segmentation result. The F1-score or Dice similarity coefficient states how the predicted segmented region matches the GT in location and level of details and considers each class’s false alarm and missed value. This metric determines the accuracy of the segmentation boundaries [32] and have a higher priority than the Acc. Another common and essential evaluation metric for semantic image segmentation is the Jaccard similarity index known as Intersection over Union (IoU). This metric is a correlation among the prediction and GT [17, 33], and represents the overlap and union area ratio for the predicted

and GT segmentation.

$$\text{Acc} = \frac{\text{Correctly Predicted Pixels}}{\text{Total Number of Image Pixels}} = \frac{\text{TP} + \text{TN}}{\text{TP} + \text{FP} + \text{FN} + \text{TN}} \quad (2)$$

$$\text{Pre} = \frac{\text{Correctly Predicted Cell Pixels}}{\text{Total Number of Predicted Cell Pixels}} = \frac{\text{TP}}{\text{TP} + \text{FP}} \quad (3)$$

$$\text{Recl} = \frac{\text{Correctly Predicted Cell Pixels}}{\text{Total Number of Actual Cell Pixels}} = \frac{\text{TP}}{\text{TP} + \text{FN}} \quad (4)$$

$$\text{Dice} = \frac{2 \times \text{Pre} \times \text{Recl}}{\text{Pre} + \text{Recl}} = \frac{2 \times \text{TP}}{2 \times \text{TP} + \text{FP} + \text{FN}} \quad (5)$$

$$\text{IoU} = \frac{|y_t \cap y_p|}{|y_t| + |y_p| - |y_t \cap y_p|} = \frac{\text{TP}}{\text{TP} + \text{FP} + \text{FN}} \quad (6)$$

### 3. Results

All three models were well trained and converged after running 100 epochs based on training/validation loss and Jaccard plots per epochs (Fig. 6). After tuning all hyperparameters with the best performance and training stability (Tab. 2), we selected such parameters values to improve the performance of the constructed models maximally. Then, we evaluated the achieved models with the test datasets. We assessed all trained models (Tab. 3) using the metrics in Eqs. 2–6.

Training the model with the simple U-Net method took the shortest run time with the lowest trainable number of parameters (Tab. 1). Compared with the Attention U-Net and Residual Attention U-Net, the run time difference is not huge in terms of increasing trainable parameters. The computational cost also did not increase dramatically compared with the acceptable improvement in the model performance. Figure 7 presents the segmentation results achieved by three different U-Net models. The simple U-Net segmentation result did not distinguish some vanished cell borders (Fig. 7–A, black circle). The Attention



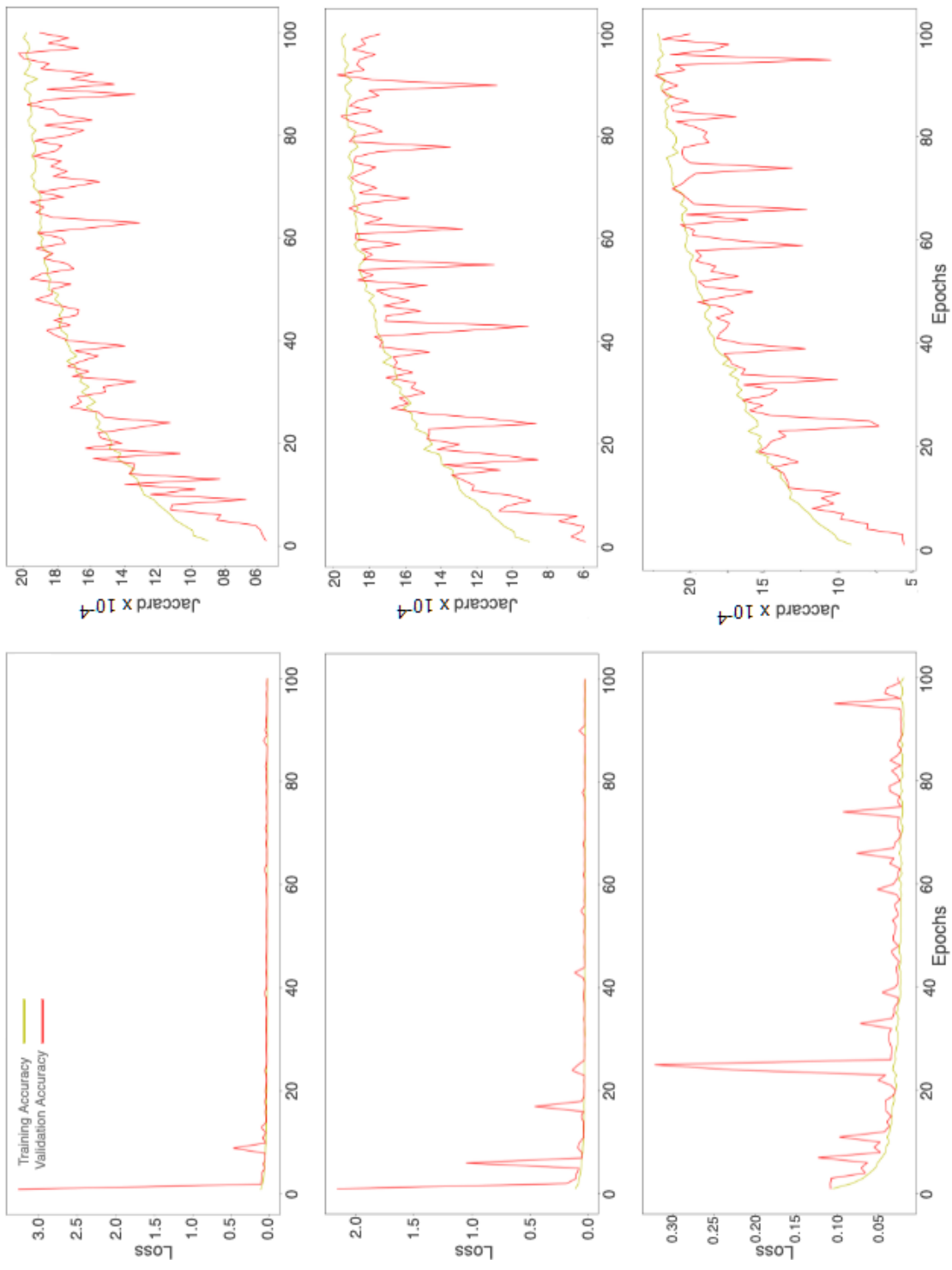


Figure 6: Training/validation plots for Simple U-Net (left column), Attention U-Net (middle column), and Residual Attention U-Net (right column).

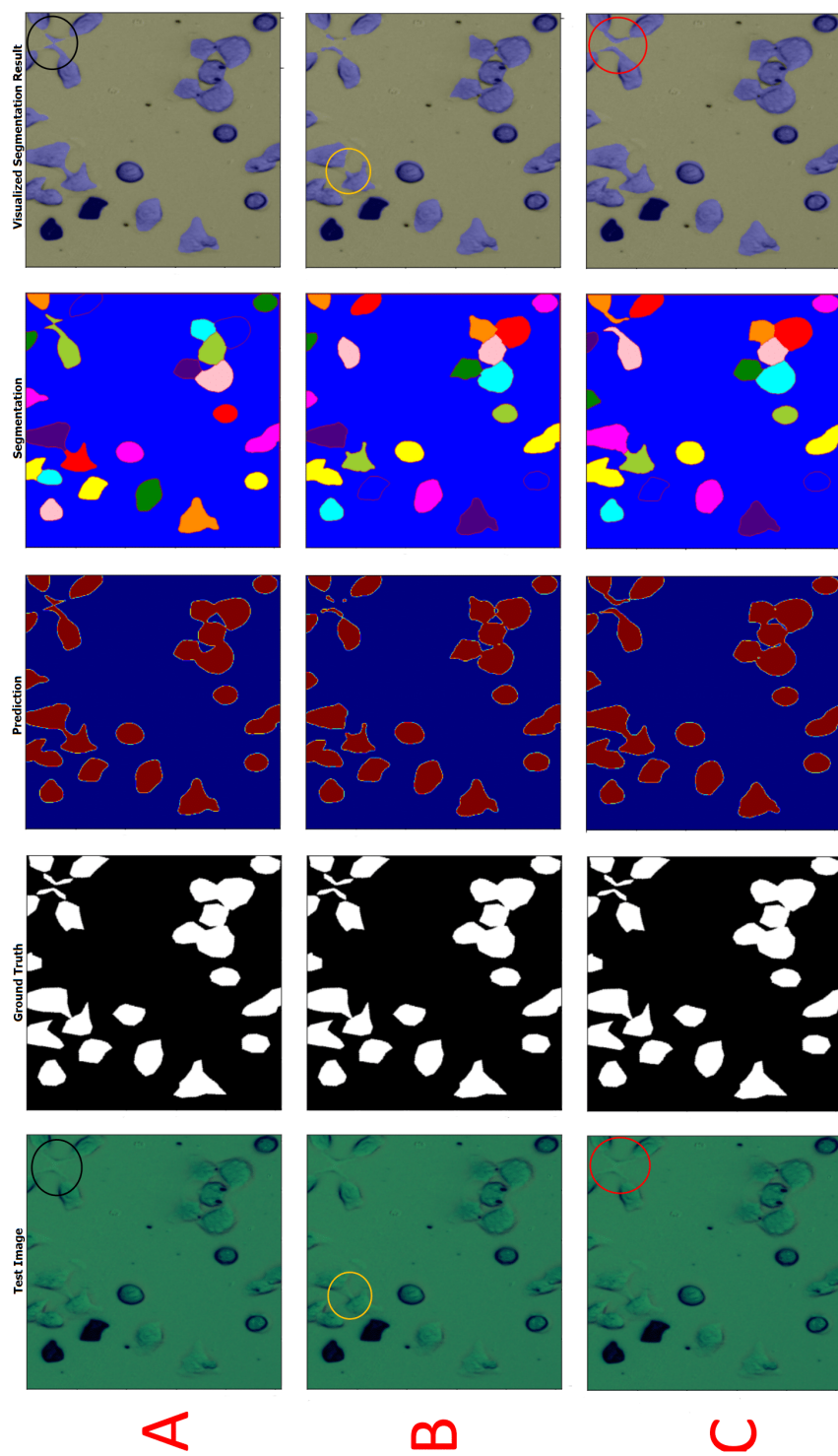


Figure 7: Segmentation results for *A*) the simple U-Net (the black circle highlights the non-segmented, vanish cell boarders), *B*) Attention U-Net (the yellow circle highlights under-segmentation problem), and *C*) the Residual Attention U-Net (red circle shows the successful segmentation of the cell boarders. The image size is  $512 \times 512$ ).

U-Net (Fig. 7–B) detected cells with the vanish borders more efficiently than the simple U-Net. However, the Attention U-net segmentation suffers from under-segmentation in some regions (visualized by the yellow circle). The outcome of the Residual Attention U-Net method (Fig. 7–C, red circle) achieved more accurate segmentation of the vanish cell borders. The watershed binary segmentation after the Residual Attention U-Net networks separated and identified the cells with the highest performance (Fig. 7).

As seen in Mean-IoU, Mean-Dice, and Accuracy metrics (Tab. 3), our Attention U-Net model showed better segmentation performance than the simple U-Net model in the same situation. After applying the residual step into the Attention U-net, we have further improved our segmentation results.

Table 3: Results for metrics evaluating the U-Net Models. Green values represent the highest segmentation accuracy for the related metric.

<b>Network</b>	<b>Accuracy</b>	<b>Precision</b>	<b>Recall</b>	<b>m-IoU</b>	<b>m-Dice</b>
<b>U-Net</b>	0.957418	0.988269	0.961264	0.950501	0.974481
<b>Attention U-Net</b>	0.959448	0.985663	0.965736	0.952471	0.975511
<b>Residual Att U-Net</b>	0.960010	0.986510	0.965574	0.953085	0.975840

#### 4. Discussion

The analysis of bright-field microscopic image sequences is challenging due to living cells’ complexity and temporal behaviour. We have to face (1) irregular shapes of the cells, (2) very different sizes of the cells, (3) noise blobs and artefacts, and (4) vast sizes of the time-lapse datasets. Traditional machine learning methods, including random forests and support vector machines, cannot deal with some of these difficulties in terms of higher computational cost and longer run time for huge time-lapse datasets. The traditional methods suffer from low performance in vanishing and tight cell detection and segmentation and are sensitive to training steps [34, 11]. The DL methods have been rapidly developed to overcome these problems. The U-Net is one of the most effective semantic segmentation methods for microscopic and biomedical images [19]. This method

is based on the FCN architecture and consists of encoder and decoder parts with many convolution layers.

The image data used to train the Residual Attention model are specific due to the way by which we obtained it. Firstly, we calibrated the optical path to obtain the number of photons that reaches each camera pixel with increasing illumination light intensity. This gave a calibration curve (image pixel intensity vs the number of photons reaching the relevant camera pixel) to correct the digital image pixel intensity. This step ensured homogeneity in digital image intensities to improve the quality of cell segmentation by the neural networks. We deal with the low-compressed telecentric transmitted light bright-field high-pixel microscopy images. The bright-field light microscope allows us to observe living cells in their most physiological state. Due to the object-sided telecentric objective, the final digital raw image of the observed cells is high-resolved and low-distorted, with no light interference halos around objects.

The procedure compressed the raw colour images ensured the least information loss at the quarter-resolution decrease. Despite the next pixel resolution decreasing, the final pixel resolution of the images that are input into the neural network is higher ( $512 \times 512$ ) than in the case of any other neural network datasets. While we try to maintain the image high resolution as much as possible, this fact arises requirements for neural network computing memory and performance parameters.

As our microscope and acquired microscopic data are unique, and were not used before in similar research, it is hard to compare the results with other works. Despite this, we tried to compare the performances of our U-Net-based models with similar microscopic and medical works (Tab. 4). We trained and evaluated the first model on a simple U-Net structure. We achieved the Mean-IoU score of 0.9505. We assume that our best value of mean IoU will be achieved after the hyperparameter optimization (Tab. 2). Ronnenberger et al. [19] achieved 0.920 and 0.775 Mean-IoU scores for U373 cell line in phase-contrast microscopy and HeLa cell line in Nomarski contrast, respectively. Pan et al. [35] segmented nuclei from medical, pathological MOD datasets with

0.7608 segmentation IoU accuracy score using the U-net.

To improve the U-Net model performance further, we implemented an attention gate into the U-Net structure (so-called Attention U-Net) to weigh the relevant part of the image pixels containing the target object. In this way, we improved the Mean-IoU metric to 0.9524. The achieved IoU score represents a noticeable improvement in the trained model performance compared with the simple U-Net model. To the best of our knowledge, not many researchers have applied the Attention U-Net to microscopic datasets, but recent papers are prevalently about its application to medical datasets. Microscopic and medical datasets have their complexity and structure, complicating the comparison of the method performances. Applying the Attention U-Net, pancreas [24] and liver tumour [36] medical datasets showed 0.840 and 0.948 Dice metric segmentation accuracy, respectively.

Table 4: Performances of the proposed networks and other networks proposed for microscopic and medical applications. Green highlighted value represent the highest segmentation accuracy in term of mentioned metric.

Models	IoU	Dice	Acc
<b>proposed U-Net</b>	0.9505	0.9744	0.9574
<b>proposed Att U-Net</b>	0.9524	0.9755	0.9594
<b>proposed Res_Att_U-Net</b>	0.9530	0.9758	0.9600
U-Net [19]	0.9203	0.9019	0.9554
U-Net [35]	0.7608	-	0.9235
Segnet [35]	0.7540	-	0.9225
Attention U-Net [24]	-	0.840	0.9734
Residual Attention U-Net [36]	-	0.9081	0.9557
Residual U-Net [37]	-	0.8366	-
Residual Attention U-Net [38]	-	0.9655	0.9887

We improved our model by one step and obtained the Residual Attention U-Net to overcome the vanishing gradient problem and generalization ability. As a result, we have improved the segmentation accuracy by reaching the Mean-IoU of 0.953. The Residual Attention U-Net showed the Dice coefficient of 0.9655 in the testing phase of medical image segmentation [38]. The Recurrent Residual U-Net (R2U-Net) achieved the Dice coefficient of 0.9215 in the testing phase

of nuclei segmentation [25]. Patel et al. [37] applied the Residual U-Net to bright-field absorbance image and achieved the Mean-Dice coefficient score of 0.8366.

## 5. Conclusion

Microscopic image analysis via deep learning methods can be a convenient solution due to the complexity and variability of this kind of data. This research aimed to detect and segment living human HeLa cells in images acquired using an original custom-made bright-field transmitted light microscope. We involved three types of deep learning U-net architectures: the simple U-Net, Attention U-Net, and Residual Attention U-Net. The simple U-Net (Tab. 1) has the fastest training time. On the other hand, the Residual Attention U-Net architecture achieved the best segmentation performance (Tab. 3) with a run time similar to the other two U-Net models.

The Attention U-net is a method to highlight only the relevant activations during the training process. This method can reduce the computational resource waste on irrelevant activations to generate more efficient models. Due to the integration of the residual learning structure (to overcome the gradient vanishing) together with the attention gate mechanism (to integrate a low and high-level feature representation) into the U-Net architecture, we achieved the best segmentation performance. After extracting semantic segmentation binary results (Tab. 3), we applied the watershed segmentation method exemplarily to separate the cells from each other, avoid the over-segmentation, label the cells individually, and extract vital information about the cells (e.g., the total number of the segmented cells, cell equivalent diameter, mean intensity and solidity). Nevertheless, future works are still essential to expand the knowledge on multi-class semantic segmentation with different and efficient CNN's architecture and combine the constructed CNN models in the prediction process to achieve the most accurate segmentation result.

## FUNDING

This work was supported by the Ministry of Education, Youth and Sports of the Czech Republic – projects CENAKVA (LM2018099) and from the European Regional Development Fund in frame of the project ImageHeadstart (ATCZ215) in the Interreg V-A Austria–Czech Republic programme. The work was further financed by the project GAJU 017/2016/Z.

## DECLARATION OF COMPETING INTEREST

The authors declare no conflict of interest, or known competing financial interests, or personal relationships that could have appeared to influence the work reported in this paper.

## ACKNOWLEDGEMENT

The authors would like to thanks our lab colleagues Šárka Beranová and Pavlína Tláskalová (all from ICS USB) and Mohammad Mehdi Ziaei for their support of this study.

## References

- [1] R. Rojas-Moraleda, W. Xiong, N. Halama, K. Breitkopf-Heinlein, S. Dooley, L. Salinas, D. W. Heermann, N. A. Valous, Robust detection and segmentation of cell nuclei in biomedical images based on a computational topology framework, *Med. Image Anal.* 38 (2017) 90–103. doi:10.1016/j.media.2017.02.009.
- [2] J. R. Tang, N. A. M. Isa, E. S. Ch'ng, A fuzzy-c-means-clustering approach: Quantifying chromatin pattern of non-neoplastic cervical squamous cells, *PLoS ONE* 10 (11). doi:10.1371/journal.pone.0142830.
- [3] Z. Wang, A semi-automatic method for robust and efficient identification of neighboring muscle cells, *Pattern Recogn.* 53 (2016) 300–312. doi:10.1016/j.patcog.2015.12.009.

- [4] G. Fan, J.-W. Zhang, Y. Wu, D.-F. Gao, Adaptive marker-based watershed segmentation approach for t cell fluorescence images, in: 2013 International Conference on Machine Learning and Cybernetics, Vol. 02, 2013, pp. 877–883. doi:10.1109/ICMLC.2013.6890407.
- [5] P. P. Guan, H. Yan, Blood cell image segmentation based on the hough transform and fuzzy curve tracing, in: 2011 International Conference on Machine Learning and Cybernetics, Vol. 4, 2011, pp. 1696–1701. doi:10.1109/ICMLC.2011.6016961.
- [6] X. Zhou, F. Li, J. Yan, S. T. Wong, Novel cell segmentation method and cell phase identification using markov model, *IEEE Trans. Inf. Technol. Biomed.* 13 (2) (2009) 152–157. doi:10.1109/TITB.2008.2007098.
- [7] M. Winter, W. Mankowski, E. Wait, E. C. D. L. Hoz, A. Aguinaldo, A. R. Cohen, Separating touching cells using pixel replicated elliptical shape models, *IEEE Trans. Med. Imaging* 38 (4) (2019) 883–893. doi:10.1109/TMI.2018.2874104.
- [8] F. Buggenthin, C. Marr, M. Schwarzfischer, P. S. Hoppe, O. Hilsenbeck, T. Schroeder, F. J. Theis, An automatic method for robust and fast cell detection in bright field images from high-throughput microscopy, *BMC Bioinform.* 14 (2013) 297. doi:10.1186/1471-2105-14-297.
- [9] S. J. Russell, *Artificial Intelligence: A Modern Approach*, Third Edition, Prentice Hall, 2010.
- [10] F. Mualla, S. Schöll, B. Sommerfeldt, A. K. Maier, J. Hornegger, Automatic cell detection in bright- field microscope images using SIFT, random forests, and hierarchical clustering, *IEEE Trans. Med. Imaging* 32 (12) (2013) 2274–2286. doi:10.1109/TMI.2013.2280380.
- [11] T. Tikkanen, P. Ruusuvoori, L. Latonen, H. Huttunen, Training based cell detection from bright-field microscope images, in: 2015 9th International



- Symposium on Image and Signal Processing and Analysis (ISPA), 2015, pp. 160–164. doi:10.1109/ISPA.2015.7306051.
- [12] G. Hinton, T. Sejnowski, *Unsupervised Learning: Foundations of Neural Computation*, MIT Press, MIT Press, 1999.
- [13] F. Mualla, S. Schöll, B. Sommerfeldt, A. Maier, S. Steidl, R. Buchholz, J. Hornegger, Unsupervised unstained cell detection by SIFT keypoint clustering and self-labeling algorithm, in: P. Golland, N. Hata, C. Barillot, J. Hornegger, R. Howe (Eds.), *Medical Image Computing and Computer-Assisted Intervention – MICCAI 2014. Lecture Notes in Computer Science*, Vol. 8675, Springer International Publishing, Cham, 2014, pp. 377–384. doi:10.1007/978-3-319-10443-0\_48.
- [14] R. Girshick, J. Donahue, T. Darrell, J. Malik, Rich feature hierarchies for accurate object detection and semantic segmentation, in: *IEEE conference on computer vision and pattern recognition*, 2014, pp. 580–587. doi:10.1109/CVPR.2014.81.
- [15] Y. Song, L. Zhang, S. Chen, D. Ni, B. Lei, T. Wang, Accurate segmentation of cervical cytoplasm and nuclei based on multiscale convolutional network and graph partitioning, *IEEE Trans. Biomed.* 62 (10) (2016) 2421–2433. doi:10.1109/TBME.2015.2430895.
- [16] F. Xing, Y. Xie, L. Yang, An automatic learning-based framework for robust nucleus segmentation, *IEEE Trans. Med. Imaging* 35 (2) (2016) 550–566. doi:10.1109/TMI.2015.2481436.
- [17] J. Long, E. Shelhamer, T. Darrell, Fully convolutional networks for semantic segmentation, in: *IEEE conference on computer vision and pattern recognition*, 2015, pp. 3431–3440. doi:10.1109/CVPR.2015.7298965.
- [18] A. Ben-Cohen, I. Diamant, E. Klang, M. Amitai, H. Greenspan, Fully convolutional network for liver segmentation and lesions detection in deep learning and data labeling for medical applications, in: G. Carneiro,

- D. Mateus, L. Peter (Eds.), Deep Learning and Data Labeling for Medical Applications DLMIA 2016, LABELS 2016. Lecture Notes in Computer Science, Vol. 10008, Springer, Cham, 2016, pp. 77–85. doi:10.1007/978-3-319-46976-8\_9.
- [19] O. Ronneberger, P. Fischer, T. Brox, U-Net: Convolutional networks for biomedical image segmentation, in: N. Navab, J. Hornegger, W. Wells, A. Frangi (Eds.), Medical Image Computing and Computer-Assisted Intervention – MICCAI 2015. Lecture Notes in Computer Science, Vol. 9321, Springer, Cham, 2015, pp. 234–241. doi:10.1007/978-3-319-24574-4\_28.
- [20] W. Liu, A. Rabinovich, A. C. Berg, Parsenet: Looking wider to see better, CoRR.
- [21] G. Platonova, D. Štys, P. Souček, K. Lonhus, J. Valenta, R. Rychtáriková, Spectroscopic approach to correction and visualization of bright-field light transmission microscopy biological data, Photonics 8 (8) (2021) 333. doi:10.3390/photonics8080333.
- [22] D. Štys, T. Náhlík, P. Macháček, R. Rychtáriková, M. Saberioon, Least information loss (LIL) conversion of digital images and lessons learned for scientific image inspection, in: F. Ortuno, I. Rojas (Eds.), Bioinformatics and Biomedical Engineering. IWBBIO 2016. Lecture Notes in Computer Science, Vol. 9656, Springer, Cham, 2016, pp. 527–536. doi:10.1007/978-3-319-31744-1\_47.
- [23] A. Buades, B. Coll, J.-M. Morel, A non-local algorithm for image denoising, in: 2005 IEEE Computer Society Conference on Computer Vision and Pattern Recognition (CVPR’05), Vol. 2, 2005, pp. 60–65. doi:10.1109/CVPR.2005.38.
- [24] O. Oktay, J. Schlemper, L. L. Folgoc, M. Lee, M. Heinrich, K. Misawa, K. Mori, S. McDonagh, N. Y. Hammerla, B. Kainz, B. Glocker, D. Rueckert, Attention U-Net: Learning where to look for the pancreas, in: 1st

- Conference on Medical Imaging with Deep Learning (MIDL 2018), 2018, pp. –.
- [25] M. Z. Alom, C. Yakopcic, T. M. Taha, V. K. Asari, Nuclei segmentation with recurrent residual convolutional neural networks based U-Net (R2U-Net), in: IEEE National Aerospace and Electronics Conference (NAECON 2018), 2018, pp. 228–233. doi:10.1109/NAECON.2018.8556686.
- [26] W. Zhang, D. Jiang, The marker-based watershed segmentation algorithm of ore image, in: 2011 IEEE 3rd International Conference on Communication Software and Networks, 2011, pp. 472–474. doi:10.1109/ICCSN.2011.6014611.
- [27] N. Otsu, A threshold selection method from gray-level histograms, IEEE Transactions on Systems, Man, and Cybernetics 9 (1) (2015) 62–66. doi:10.1109/TSMC.1979.4310076.
- [28] M. Abadi, A. Agarwal, P. Barham, E. Brevdo, Z. Chen, C. Citro, TensorFlow: large-scale machine learning on heterogeneous distributed systems, in: OSDI'16: Proceedings of the 12th USENIX conference on Operating Systems Design and Implementation, 2016, pp. 265–283.
- [29] Google, System spec.  
URL <https://research.google.com/colaboratory/faq.html>
- [30] T. Lin, P. Goyal, R. Girshick, K. He, P. Dollár, Focal loss for dense object detection, IEEE Trans. Pattern Anal. Mach. Intell. 42 (2) (2020) 318–327. doi:10.1109/TPAMI.2018.2858826.
- [31] X. Pan, L. Li, H. Yang, Z. Liu, J. Yang, Y. Fan, Accurate segmentation of nuclei in pathological images via sparse reconstruction and deep convolutional networks, Neurocomputing 229 (2017) 88–99. doi:10.1016/j.neucom.2016.08.103.

- [32] G. Csurka, D. Larlus, F. Perronnin, What is a good evaluation measure for semantic segmentation?, in: British Machine Vision Conference 2013, 2013, pp. 32.1–32.11. doi:10.5244/C.27.32.
- [33] B. Vijay, A. Kendall, R. Cipolla, SegNet: A deep convolutional encoder-decoder architecture for image segmentation, IEEE Trans. Pattern Anal. Mach. Intell. 39 (12) (2015) 228–233. doi:10.1109/TPAMI.2016.2644615.
- [34] C. Sommer, C. Straehle, U. Köthe, F. A. Hamprecht, Ilastik: Interactive learning and segmentation toolkit, in: 2011 IEEE International Symposium on Biomedical Imaging: From Nano to Macro, 2011, pp. 230–233. doi:10.1109/ISBI.2011.5872394.
- [35] X. Pan, L. Li, D. Yang, Y. He, Z. Liu, H. Yang, An accurate nuclei segmentation algorithm in pathological image based on deep semantic network, IEEE Access 7 (2019) 110674–110686. doi:10.1109/ACCESS.2019.2934486.
- [36] Z. Wang, Y. Zou, P. X. Liu, Hybrid dilation and attention residual U-Net for medical image segmentation, Comput. Biol. Med. 134 (2021) 104449. doi:10.1016/j.combiomed.2021.104444.
- [37] G. Patel, H. Tekchandani, S. Verma, Cellular segmentation of bright-field absorbance images using residual u-net, 2019 International Conference on Advances in Computing, Communication and Control (ICAC3) (2019) 1–5doi:10.1109/ICAC347590.2019.9036737.
- [38] J. Qiangguo, M. Zhaopeng, S. Changming, C. Hui, S. Ran, RA-UNet: A hybrid deep attention-aware network to extract liver and tumor in CT scans, Front. Bioeng. Biotechnol. 8 (2020) 1471. doi:10.3389/fbioe.2020.605132.